Influence of Fröhlich Interaction on Intersubband Transitions of InGaAs/InAlAs-Based Quantum Cascade Detector Structures Investigated by Infrared Modulated Photoluminescence

Liangqing Zhu(朱亮清)[1†*], Shuman Liu(刘舒曼)[2†], Jun Shao(邵军)[3*], Xiren Chen(陈熙仁)[3], Fengqi Liu(刘峰奇)[2], Zhigao Hu(胡志高)[1], and Junhao Chu(褚君浩)[1,3]

[1]*Technical Center for Multifunctional Magneto-Optical Spectroscopy (Shanghai), School of Physics and Electronic Science, East China Normal University, Shanghai 200241, China*
[2]*Key Laboratory of Semiconductor Materials Science, Institute of Semiconductors, Chinese Academy of Sciences, Beijing 100083, China*
[3]*National Laboratory for Infrared Physics, Shanghai Institute of Technical Physics, Chinese Academy of Sciences, Shanghai 200083, China*

(Received 21 February 2023; accepted manuscript online 29 May 2023)

We demonstrate the use of an infrared modulated photoluminescence (PL) method based on a step-scan Fourier-transform infrared spectrometer to analyze intersubband transition (ISBT) of InGaAs/InAlAs quantum cascade detector (QCD) structures. By configuring oblique and parallel excitation geometries, high signal-to-noise ratio PL spectra in near-to-far-infrared region are measured. With support from numerical calculations based on the $\boldsymbol{k}\cdot\boldsymbol{p}$ perturbation theory, the spectra is attributed to intraband and interband transitions of InGaAs/InAlAs QCD structures. Temperature evolution results show that the k-dependent transitions caused by longitudinal optical phonon-assisted scattering (Fröhlich interaction) plays an important role in the ISBT. These results suggest that this infrared modulated-PL method has great potential in characterizing QCD devices and conducting performance diagnostics.

DOI: 10.1088/0256-307X/40/7/077503

Quantum cascade detectors (QCDs) are one of the most promising types of tailorable photovoltaic devices, principally because their wavelength range, starting from short wavelengths up to those of terahertz waves and through the entire infrared band, is suitable for many military and commercial applications.[1–5] The functioning of QCDs is based on intersubband (ISB) transitions in periodic multiple quantum wells (QWs) made of semiconducting materials. The crucial design aspect of QCDs introduces an asymmetry in the conduction band profile that provides a preferential escape direction and leads to a net measurable photocurrent without any external bias voltage.[6–11] Thus the photovoltaic work mechanism of QCDs guarantees zero dark current, which allows the QCDs to excel in regard to signal-to-noise ratio (SNR) behavior, reduced thermal loading, and in simpler readout circuitry. However, recent results show that achievements of high detectivity and high-operating temperatures are still limited because of low device resistance.[12–16] Further work is therefore necessary on improving QCD-device performance, especially characterization of actual stair-like subband structures.

In the case of multiple heterostructures, optical phonons can be strongly influenced by the presence of heterointerfaces, and their interaction with two-dimensional confined electrons will be significantly modified compared with the three-dimensional case.[17–19]

The quantum-mechanical polarization selection rule states that only the electric field component perpendicular to the quantum well layers interacts with intersubband transitions, thus there are limited ways to characterize band structures of QCD devices without modifying the device geometries. Current reported methods include transmission spectroscopy,[6,20,21] photocurrent (PC) spectroscopy,[15,22] and electroreflectance (ER).[23] For transmission spectroscopy, QCD samples need to be polished into 45° multipass waveguides to improve the coupling efficiency of the incident probe, which increases the difficulty of sample preparation for transmission measurements.[20] For PC spectroscopy, the preparation of specific geometry devices, such as photolithography, wet etching, and evaporating metal contacts,[24] is also cumbersome but a larger problem is the heating effect and/or carrier depletion of ground states caused by the applied DC bias may disturb the characterization of QCD subbands. Consequently, the above two methods are difficult or unreliable when characterizing QCD subbands. ER is one of the forms of modulation spectroscopy that has been successfully applied in studying the subband structure of quantum cascade lasers (QCLs).[23] However, the internal perturbed electric field in the ER measurement conflicts with the zero bias operation mode of QCDs. Hence, ER is also unsuitable for characterizing QCD subbands.

Photoluminescence (PL) spectroscopy, as a non-contact non-destructive optical method, is convenient and

†These authors contributed equally to this work.
*Corresponding authors. Email: lqzhu@ee.ecnu.edu.cn; jshao@mail.sitp.ac.cn
© 2023 Chinese Physical Society and IOP Publishing Ltd

powerful for probing band structure and impurity levels for a wide variety of semiconductors. The PL measurement does not require external bias voltages and micromachining of the electrode contacts. It overcomes the shortcomings of PC and ER methods in characterization of the QCD subbands. Moreover, the PL spectra not only probes band structures of QCDs, but also extract phonon-assisted scattering effects on the preferential transport of electrons in the QCD subbands through the temperature evolution of the PL spectra. Hence, PL method is more effective in characterizing subband structures of QCD devices. Up to date, however, there has been no prior report on characterization of QCDs, except for QWs or superlattices.[25–27] The reasons may be that (i) the conventional PL measurement is limited to visible and near-infrared regions, for which wavelengths are shorter than the typical wavelengths associated with QCD subband transitions, (ii) the radiative recombination efficiency of the intraband transitions is usually much lower than that of interband transitions, and (iii) the subband PL of the QCD structure has special requirements regarding geometric configuration.

In this Letter, we describe temperature-dependent PL measurements for InGaAs/InAlAs QCD structures, which improve the sensitivity and SNR upon our previously established modulated-PL method based on a step-scan Fourier-transform infrared (FTIR) spectrometer.[28–32] Moreover, to strengthen the PL signal of QCD intraband transitions, both oblique and parallel excitation geometries that refer to the growth plane of the QCD are applied in the PL measurements. Infrared PL spectra (from about 1.3 μm to 12 μm), corresponding to the intraband transitions and interband transitions of QCDs, as supported by numerical calculations based on the $\boldsymbol{k}\cdot\boldsymbol{p}$ perturbation theory, are acquired with a significantly improved SNR over a wide temperature range of 5–180 K. The temperature evolution of the PL spectra shows that with phonon-assisted scattering, intraband PL is more stable than interband PL, suggesting the infrared modulated-PL method to be of great potential in characterizing QCD devices.

Two InGaAs/InAlAs QCD samples (G846 and G858) we used were grown by molecular beam epitaxy (MBE) on Fe-doped semi-insulating (SI) InP substrates. The active region of G846 sample is based on the lattice-matched $In_{0.53}Ga_{0.47}As/In_{0.52}Al_{0.48}As$ alloy pair with designed detection of about 10.6 μm; the layer sequence of one period of the structure is 10.0/**4.7**/3.9/**2.5**/4.3/**1.9**/5.4/**1.6**/6.6/**1.7** nm. The active region of the G858 sample is based on the strain-compensated $In_{0.6}Ga_{0.4}As/In_{0.45}Al_{0.55}As$ alloy pair with designed detection of about 4.3 μm, for which each period comprises <u>4.5</u>/**4.0**/3.3/**2.6**/2.7/**3.0**/2.2/**3.0**/1.9/**3.5**/1.6/**4.0**/1.3/**5.0**/1.0/**6.0** nm. Barrier layers ($In_{0.52}Al_{0.48}As$ or $In_{0.45}Al_{0.55}As$) are in bold, and well layers ($In_{0.53}Ga_{0.47}As$ or $In_{0.6}Ga_{0.4}As$) are in Roman. Underlined numbers are n-doped layers (Si, 1×10^{18} cm^{-3}).[8,13,14,33] The active region of each sample is repeated by 30 periods. The design optimization of the above InGaAs/InAlAs QCD structures is based on our earlier research, which indicates that increasing the number of cascade stages and reducing the thickness of the barrier can enhance QCD device responsivity and operating temperature, while hardly affect detection capability.[33]

Following procedures for the modulated PL method, measurements were performed using the step-scan FTIR spectrometer (Bruker Vertex 80v),[28,29,31,32] in combination of an uncooled InGaAs detector to probe the PL signal of the interband transitions, a liquid-nitrogen cooled photovoltaic HgCdTe detector to probe the PL signal of the intraband transitions, and a KBr beam splitter. The spectral resolution was 6 cm^{-1} (or equivalently, 0.75 meV). The temperature of the sample was regulated using a close-cycle cryostat. The excitation source was a combination of laser-power controller and a 532 nm diode laser with a spot diameter of about 50 μm on the sample surface using apertures and lenses. To enhance the PL signal of the QCD intraband transitions, the samples were excited by a laser in both oblique (denoted by O-PL) and parallel (denoted by P-PL) geometries relative to the growth plane of the QCD device.

From the high-energy PL spectrum associated with interband transition of the G846 sample excited in the oblique geometry (see inset) at $T = 5$ K [Fig. 1(a)], there is a major peak in the interband PL spectrum, labeled as peak A. Its energy is about 0.78 eV (or equivalently, 1.57 μm), but its shape is asymmetric, implying that it contains multiple transitions among the energy levels. The low energy (mid-infrared) PL spectrum of the G846 sample excited in the oblique geometry (see inset) at $T = 5$ K [Fig. 1(b)] show three peaks in the range from about 0.07 eV to 0.7 eV, located at about 0.12 eV (10.3 μm), 0.35 eV, and 0.43 eV (2.8 μm), respectively. Referring to the existing literature,[34,35] the sharp asymmetric PL feature of the 0.35 eV peak is derived from an internal transition of the Fe^{2+} ion ($^5T_2 \rightarrow {}^5E$) in the InP substrate. However, there are no transitions corresponding to the remaining two broad symmetric PL features (at about 0.43 eV and 0.12 eV) in the InP substrate. Therefore, we believe that these two unknown PL features, labeled as peaks B (0.43 eV) and C (0.12 eV), respectively, come from intraband transitions within the conduction band in the QCD region of the G846 sample.

Figures 1(c) and 1(d) show, respectively, the interband and intraband PL spectra of the G858 sample excited in both oblique and parallel geometries (see insets) at $T = 5$ K. For both geometries the energy of the interband PL peak (labeled peak D) is about 0.82 eV (1.49 μm) and its shape depends on the excitation geometry. For the intraband, two overlapping PL peaks are in a narrow range of about 0.32 eV to 0.35 eV for both oblique and parallel geometries (magenta dashed box, labeled by X). The one peak located at 0.35 eV has been assigned to the PL signal of the Fe^{2+} ion from the InP substrate. The other peak (labeled as peak E) located at about 0.34 eV (3.7 μm) is difficult to distinguish clearly in the oblique geometry because the PL signal of the Fe^{2+} ion is strong. However, the intensity ratio of peak E to the Fe^{2+} ion PL signal increases in parallel geometry. The inference is that peak E does not come from an internal transition of the Fe^{2+} ion and is unrelated to the InP substrate. Support for this viewpoint is seen in the upper inset of Fig. 1(d), which reveals a temperature dependence of the PL spectra of the InP substrate in the range from 0.27 eV to 0.37 eV, show-

ing that the Fe^{2+} ion PL decreases rapidly with increasing temperature and almost disappears at 77 K. The lower inset shows the temperature-dependent PL spectra of the G858 sample in parallel geometry and demonstrates that the Fe^{2+} PL also decreases rapidly as temperature rises. Nevertheless, the reduction for peak E is very slow from 5 K to 77 K. These results confirm that the PL mechanism of peak E is not related to the Fe^{2+} ions. In addition, according to the polarization selection rule of quantum optics, the enhancement in peak E in the parallel geometry arises from the strengthening of the interaction between the laser electric field component and the intersubband transitions. Hence, we deduce that peak E originates from the intraband transition of the QCD region in the G858 sample.

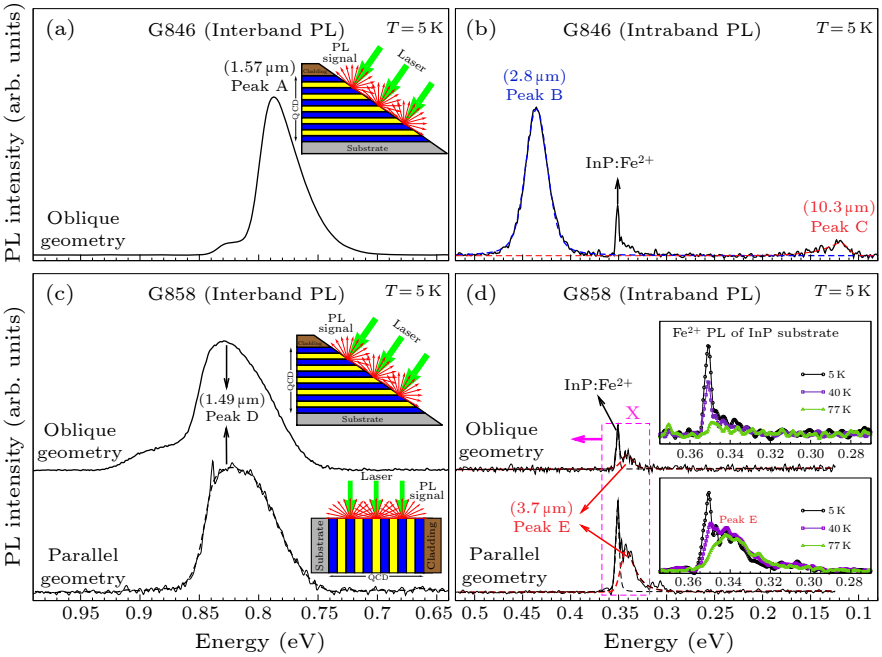

Fig. 1. [(a), (b)] The interband PL and (conduction band) intraband PL of the G846 sample excited in the oblique geometry at $T = 5$ K, respectively. [(c), (d)] The interband PL and (conduction band) intraband PL of the G858 sample excited in both oblique and parallel geometries at $T = 5$ K, respectively.

To further verify the origin of the observed PL features (peaks A, B, C, D, and E), we compare these PL peaks to those calculated from the QCDs band structure. The band-structure model of the QCDs we used is based on an envelope function approach in the Burt–Foreman theory introduced in Ref. [36]. The total wave function is expanded in terms of band-edge ($k = 0$) Bloch functions u_n,

$$\Psi(\boldsymbol{r}) = \sum_n F_n(\boldsymbol{r}) u_n(\boldsymbol{r}),$$
$$F_n = \exp[i(k_{\mathrm{SL}} \cdot z)] \exp[i(k_x x + k_y y)] f_n(z), \quad (1)$$

where $F_n(\boldsymbol{r})$ represents the envelope functions, $u_n(\boldsymbol{r})$ is assumed to be the same in the barrier and well layers of the QCD, $k_{\mathrm{SL}} \in [-\pi/L_z, \pi/L_z]$ is the wave vector of the QCD superlattice (along z-axis) and a good quantum number, L_z is the thickness of one period of the QCD structure, k_x and k_y are the wave vector components in the x–y plane of the QCD, and $f_n(z) = f_n(z + L_z)$ are slowly varying envelope functions.

The conduction-subband dispersion is calculated using the effective mass approximation (EMA) model, in which the nonparabolicity of the conduction band is considered in the Schrödinger equation with an energy-dependent effective electron mass characterized by a modified Kane formula as follows:[37]

$$\Big[-\frac{\hbar^2(k_z + k_{\mathrm{SL}})^2}{2m_{\mathrm{e}}^*(z,E)} + \frac{\hbar^2 k_\parallel^2}{2m_{\mathrm{e}}^*(z,E)} + V_{\mathrm{e}}(z)\Big] f_n^{\mathrm{e}}(z) = E(k_\parallel, k_{\mathrm{SL}}) f_n^{\mathrm{e}}(z),$$
$$\frac{m_0}{m_{\mathrm{e}}^*(z,E)} = 1 + \frac{2m_0 P(z)^2}{3\hbar^2}\Big(\frac{2}{E_{\mathrm{g}}(z)+E} + \frac{1}{E_{\mathrm{g}}(z)+\Delta+E}\Big), \quad (2)$$

where $k_\parallel = k_x\hat{x} + k_y\hat{y}$, $f_n^{\mathrm{e}}(z) = f_n^{\mathrm{e}}(z + L_z)$, $V_{\mathrm{e}}(z) = V_{\mathrm{e}}(z + L_z)$ is the potential function of electrons, $P(z)$ and $E_{\mathrm{g}}(z)$ are Kane's momentum matrix element and the bandgap of the QCD material, respectively, at position z.

The valence-subband dispersions are calculated using the Luttinger–Kohn model[38] based on the 6×6 $\boldsymbol{k}\cdot\boldsymbol{p}$ perturbation theory, in which biaxial strain caused by lattice mismatch (the G858 sample) and the spin-orbit (SO) interaction are considered. Meanwhile, the variation of the conduction (valence) band offset with strain and temperature has been taken into account in determining the confining potentials by applying the Bir–Pikus Hamiltonian[39] and using the Varshni equation.[40] The band parameters used for the InGaAs and InAlAs ternary alloys, including the band-gap (E_{g}), the effective electron mass (m_{e}^*),

the Luttinger–Kohn parameters (γ_1, γ_2, γ_3, κ), the SO split-off energy ($\Delta_{\rm SO}$), the hydrostatic band deformation potentials and elastic constants (a_c^Γ, $a_{v,av}$, b, d, c_{11}, c_{12}, c_{44}), are referenced in the review of Vurgaftman *et al.*[40] In calculations, we assume $\gamma_2 = \gamma_3$ under the axial approximation.

The envelope functions and the energy levels of electron and/or hole near $\boldsymbol{k}_\parallel = 0$ and/or $\boldsymbol{k}_{\rm SL} = 0$ are determined within the framework of $\boldsymbol{k}\cdot\boldsymbol{p}$ theory by replacing k_z with $-i\frac{\partial}{\partial z}$ and solving the resulting differential matrices. To numerically solve the eigenvalue problem of these matrices, the envelope functions $f_n(z)$ are expanded in terms of the complete basis set $\{L_i(z)\}$ under periodic boundary conditions based on the spectral method,[41]

$$f_n(z) = \sum_i c_n^i L_i(z), \quad i = 0, 1, 2, \ldots, \tag{3}$$

where $L_i(z)$ represents integrated Legendre polynomials derived from Legendre polynomials and the maximum value of i defines the accuracy of the solution of the eigenvalue problem. Equation (3) automatically satisfies the flux conserving boundary conditions which require the continuity of $f_n(z)$ and $(1/m^*)df_n(z)/dz$.

$$L_i(x) = \int_{-1}^{x} l_{i-1}(s)ds, \quad (i \geq 2), \tag{4}$$

where $l_{i-1}(s)$ is Legendre polynomials, for completeness we add $L_0(x) = -1$ and $L_1(x) = x$. Polynomials usually up to 15 order are sufficient to the high accuracy. The expansion in Eq. (3) leads to a matrix representation of the eigenvalue problem of QCD band structure where the eigenvectors with components c_n^i and the corresponding eigenvalues are obtained by matrix diagonalization.

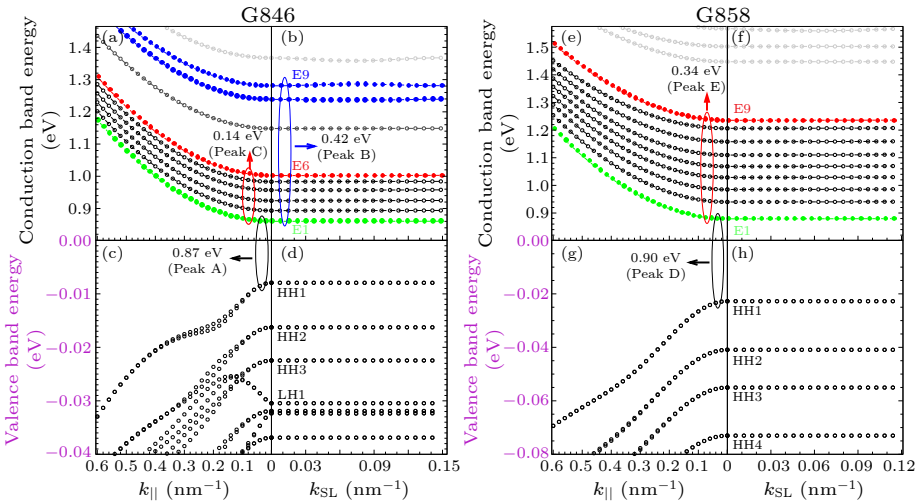

Fig. 2. Calculated in-plane ($k_\parallel$) and perpendicular ($k_{\rm SL}$) dispersion relation of the conduction-subbands and valence-subbands for G846 (left) and G858 (right) QCD samples. HH: heavy hole, LH: light hole.

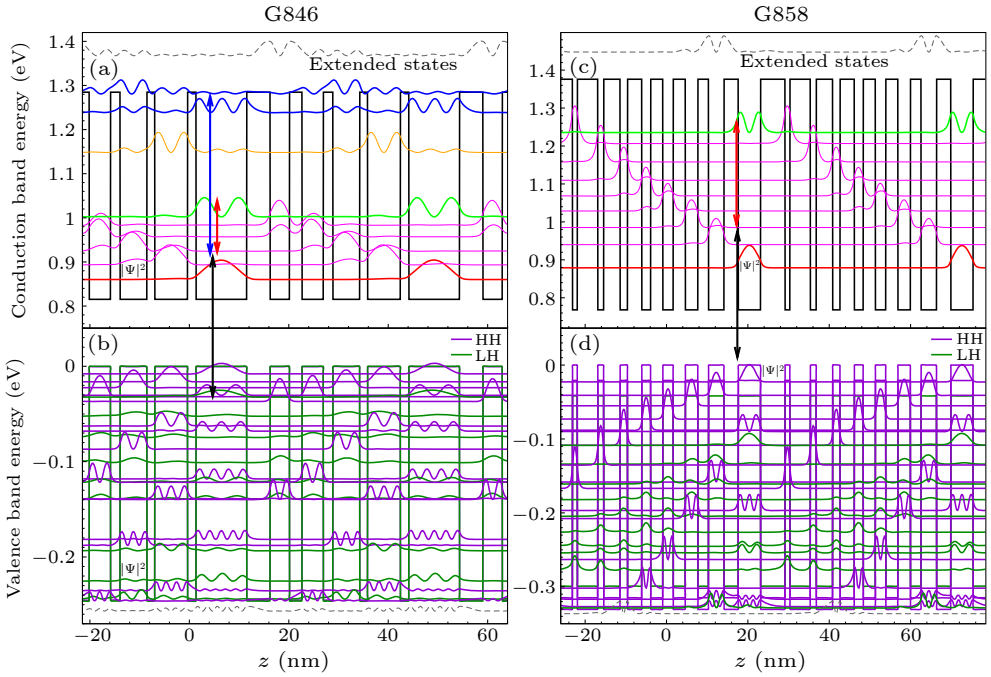

Fig. 3. The spatial distribution of the calculated electron and hole wave functions within one period of the conduction-subbands and valence-subbands for G846 (left) and G858 (right) QCD samples at $k_{\rm SL} = 0$ and $k_\parallel = 0$.

Figure 2 shows the calculated in-plane ($k_{\parallel}$) and perpendicular (k_{SL}) dispersion relation of the conduction-subbands and valence-subbands for the G846 and G858 samples. Peak A (about 0.78 eV), peak B (about 0.43 eV), and peak C (about 0.12 eV) are shown to coincide with E1–HH1 (0.87 eV), E9–E1 (0.42 eV), and E6–E1 (0.14 eV) transition energies, respectively; see Figs. 2(a), 2(b), 2(c), and 2(d). Peak D (about 0.82 eV) and peak E (about 0.34 eV) fit well with E1–HH1 (0.90 eV) and E9–E1 (0.34 eV) transition energies, respectively; see Figs. 2(e), 2(f), 2(g), and 2(h). From these comparisons, good agreement between the observed PL peak positions and the numerical calculations for the QCDs suggests that our method is effective in determining the intersubband transitions of the QCD device without the applied electric field. Figure 3 shows the spatial distribution of electron and hole wavefunctions in G846 and G858 QCD samples, numerically solved by spectral method at $k_{\mathrm{SL}} = 0$ and $k_{\parallel} = 0$.

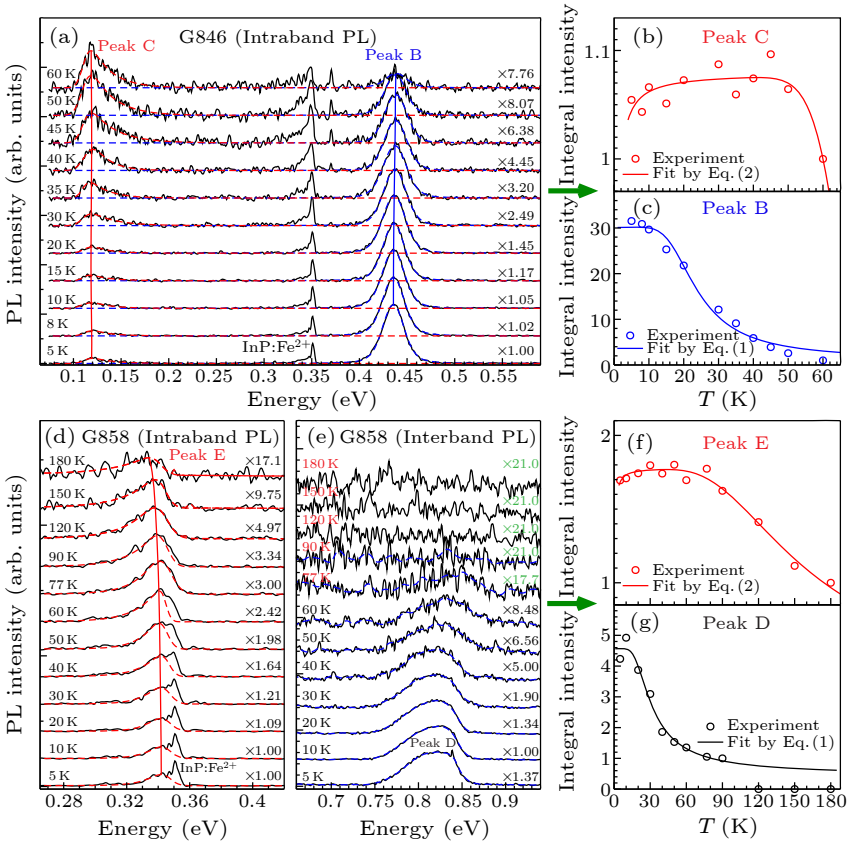

Fig. 4. Temperature evolution of the interband and intraband transitions PL of the G846 sample [(a), (b), (c)] excited in the oblique geometry and the G858 sample [(d), (e), (f), (g)] excited in parallel geometry.

To understand the influence of phonon scattering on intraband transitions of QCDs, temperature-dependent PL measurements were taken from the G846 and G858 samples. Figure 4(a) shows the temperature-dependent (5–60 K) intraband transition PL spectra (peaks B and C) of the G846 sample. Figures 4(d) and 4(e) show a comparison of the intraband transition (peak E) and interband transition (peak D) PL spectra of the G858 sample from 5 K to 180 K. Magnifications with proper factors were made to normalize the PL intensities on the right of Figs. 4(a), 4(d), and 4(e). A qualitative analysis reveals that as the temperature increases, the intensities of peaks B and D decrease rapidly whereas those of peaks C and E appear to increase initially and then decrease. A quantitative analysis of the temperature evolution behaviors for the four PL peaks [Figs. 4(b), 4(c), 4(f), 4(g)] was carried out to find that: (i) The temperature evolution curves of peaks B and D are similar and are well described by a phenomenological expression for Ⅲ–V quantum well heterostructures:[42]

$$I(T) = \frac{I_0}{1 + Ce^{-E_{\mathrm{a}}/k_{\mathrm{B}}T}}, \tag{5}$$

where I_0 is the intensity at $T = 0$ K, C the ratio between the exciton radiative lifetime in the quantum well and the exciton escape time from the quantum well to a nonradiative center, and E_{a} the thermal activation energy of the nonradiative center. (ii) The evolution curves of peaks C and E are also similar but do not satisfy Eq. (5). They can be well fitted by the modified expression

$$I(T) = e^{-\hbar\omega_0/k_{\mathrm{B}}T}\frac{I_0}{1 + Ce^{-E_{\mathrm{a}}/k_{\mathrm{B}}T}}, \tag{6}$$

where $\hbar\omega_0$ depends on the material and structural details of the sample, whereas other peaks can be fitted by Eq. (5).

Why are peaks C and E more stable than peaks B and D as temperature increases? The core reason is that the

PL mechanism of peak C/peak E is different from that of peak B/peak D. The detailed explanation is as follows. According to the conduction-subbands profiles for G846 and G858 along the growth axis calculated using the EMA model, the PL mechanism of peak B/peak D comes from the vertical transition mode between the initial and final states [see Figs. 5(a) and 5(b)]. Therefore, the temperature evolution of peaks B and D follow the normal law, i.e., Eq. (5).

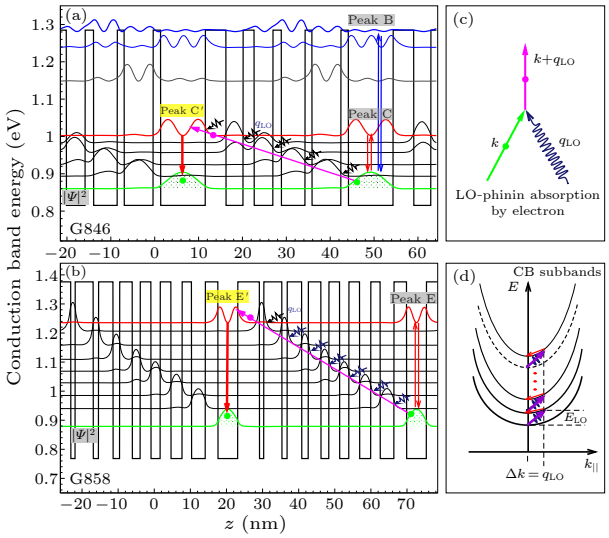

Fig. 5. [(a), (b)] Conduction-subband profiles of the respective G846 and G858 samples along the growth axis calculated using the EMA model. (c) Feynman diagram of the first-order process for electron-phonon interaction. (d) Schematic diagram of the electron multi-level k-dependent transitions assisted by LO-phonon absorption.

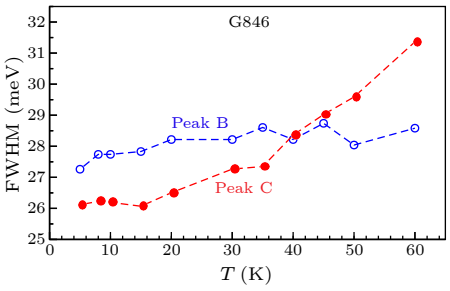

Fig. 6. Temperature evolution of FWHMs of peaks B and C (FWHM: full width at half maximum).

However, the initial and final states of peak C/peak E are located in the conduction stair-like subband of the G846/G858 sample, for which the minimum energy interval is close to the longitudinal optical (LO) phonon energy of the sample E_{LO} ($In_{0.53}Ga_{0.47}As$: $E_{LO} = 32$ meV, $In_{0.52}Al_{0.48}As$: $E_{LO} = 40$ meV, $In_{0.6}Ga_{0.4}As$: $E_{LO} = 32$ meV, $In_{0.45}Al_{0.55}As$: $E_{LO} = 41$ meV).[43] This leads to a PL mechanism for peak C/peak E that utilizes not only the vertical transition mode but also the k-dependent transition assisted by LO-phonon absorption[44,45] [see Fig. 5(c)]. For highly polar Ⅲ–Ⅴ semiconductors, the Fröhlich long-range interaction,[46] which derives from the electric dipole moment produced by the relative movement of the positive and negative ions coupling with the electron Coulomb potential, can enhance the electron-LO phonon absorption/emission multi-level k-dependent transitions [Fig. 5(d)]. It can be confirmed by the FWHM of PL peaks, as shown in Fig. 6.

The temperature evolution of the k-dependent transition mainly depends on the variation of the LO-phonon density $n(\hbar\omega_{LO})$. Because phonons are bosons, the variation of $n(\hbar\omega_{LO})$ with temperature obey Bose–Einstein statistics, $n(\hbar\omega_{LO}) \propto \frac{1}{e^{\hbar\omega_{LO}/k_B T}-1}$. At low temperatures ($k_B T \ll \hbar\omega_{LO}$), $n(\hbar\omega_{LO}) \propto e^{-\hbar\omega_{LO}/k_B T}$. This reasonably explains the factor $e^{-\hbar\omega_0/k_B T}$ in Eq. (6) for this physical mechanism. Hence, to achieve efficient electron extraction and high operating temperatures through phonon-assisted scattering, the energy difference between the individual extractor states (stair-like subband) should be close to the LO-phonon energy in the design aspect of the QCD devices.

In conclusion, we have demonstrated the possibility of using the step-scan FTIR spectrometer-based infrared modulated-PL method to detect and study intersubband transitions of InGaAs/InAlAs QCD structures. The resulting PL spectra show PL signals in near-infrared to far-infrared regions, which are attributed to intraband and interband transitions of InGaAs/InAlAs QCDs, as supported by numerical calculations based on the $\boldsymbol{k}\cdot\boldsymbol{p}$ perturbation theory. Moreover, the temperature-dependent PL results show that the long-range electron-LO phonon (Fröhlich) interaction plays an important role in intersubband transitions, which helps to increase electron extraction and the operating temperature of QCDs. This indicates that the infrared modulated-PL method offers an alternative means to characterize QCD devices and to provide performance diagnostics.

Acknowledgments. This work was supported by the National Key Research and Development Program of China (Grant No. 2019YFB2203400), the National Natural Science Foundation of China (Grant Nos. 61974044 and 11974368), and the Shanghai Committee of Science and Technology of China (Grant Nos. 20142201000 and 21ZR1421500).

References

[1] Martyniuk P, Rogalski A, and Krishna S 2022 *Phys. Rev. Appl.* **17** 027001
[2] Giparakis M, Knötig H, Detz H, Beiser M, Schrenk W, Schwarz B, Strasser G, and Andrews A M 2022 *Appl. Phys. Lett.* **120** 071104
[3] Zhou X H, Li N, and Lu W 2019 *Chin. Phys. B* **28** 027801
[4] Hillbrand J, Krüger L M, Dal C S, Knötig H, Heidrich J, Andrews A M, Strasser G, Keller U, and Schwarz B 2021 *Opt. Express* **29** 5774
[5] Bigioli A, Armaroli G, Vasanelli A, Gacemi D, Todorov Y, Palaferri D, Li L, Davies A G, Linfield E H, and Sirtori C 2020 *Appl. Phys. Lett.* **116** 161101
[6] Graf M, Hoyler N, Giovannini M, Faist J, and Hofstetter D 2006 *Appl. Phys. Lett.* **88** 241118
[7] Giorgetta F R, Baumann E, Théron R, Pellaton M, Hofstetter D, Fischer M, and Faist J 2008 *Appl. Phys. Lett.* **92** 121101
[8] Kong N, Liu J Q, Li L, Liu F Q, Wang L J, and Wang Z G 2010 *Chin. Phys. Lett.* **27** 038501

[9] Kong N, Liu J Q, Li L, Liu F Q, Wang L J, Wang Z G, and Lu W 2010 *Chin. Phys. Lett.* **27** 128503
[10] Tan Z Y, Wan W J, and Cao J C 2020 *Chin. Phys. B* **29** 084212
[11] Horiuchi N 2019 *Nat. Photon.* **13** 376
[12] Li K, Liu S M, Zhuo N, Liu J Q, Zhu Y X, Guo K, Zhai S Q, Zhang J C, Wang L J, Li Y, and Liu F Q 2022 *Appl. Phys. Express* **15** 032005
[13] Liu J Q, Wang F J, Zhai S Q, Zhang J C, Liu S M, Liu J, Wang L J, Liu F Q, and Wang Z G 2018 *Appl. Phys. Express* **11** 042001
[14] Zhou Y, Zhai S, Wang F, Liu J, Liu F, Liu S, Zhang J, Zhuo N, Wang L, and Wang Z 2016 *AIP Adv.* **6** 035305
[15] Ravikumar A P, De Jesus J, Tamargo M C, and Gmachl C F 2015 *Appl. Phys. Lett.* **107** 141105
[16] Reininger P, Schwarz B, Gansch R, Detz H, MacFarland D, Zederbauer T, Andrews A, Schrenk W, and Strasser G 2015 *Opt. Express* **23** 6283
[17] Seti J, Voitsekhivska O, Vereshko E, and Tkach M 2022 *Appl. Nanosci.* **12** 533
[18] Hofstetter D, Beck H, Epler J E, Kirste L, and Bour D P 2020 *Superlattices Microstruct.* **145** 106631
[19] Ohtani K, Meng B, Franckié M, Bosco L, Ndebeka-Bandou C, Beck M, and Faist J 2019 *Sci. Adv.* **5** eaau1632
[20] Lai K, Haywood S, Mohamed A, Missous M, and Gupta R 2005 *Appl. Phys. Lett.* **87** 192113
[21] Markmann S, Franckié M, Pal S, Stark D, Beck M, Fiebig M, Scalari G, and Faist J 2020 *Nanophotonics* **10** 171
[22] Ajili L, Scalari G, Hoyler N, Giovannini M, and Faist J 2005 *Appl. Phys. Lett.* **87** 141107
[23] Enobio E C I, Ohtani K, Ohno Y, and Ohno H 2013 *Appl. Phys. Lett.* **103** 231106
[24] Giorgetta F R, Baumann E, Graf M *et al.* 2009 *IEEE J. Quantum Electron.* **45** 1039
[25] Sauvage S, Moussa Z, Boucaud P, Julien F H, Berger V, and Nagle J 1997 *Appl. Phys. Lett.* **70** 1345
[26] Kaspi R, Tilton M L, Dente G C, Barresi R, Yang C, and Ongstad A P 2010 *Appl. Phys. Lett.* **97** 201104
[27] Łozińska A, Badura M, Bielak K, Ściana B, and Tłaczała M 2020 *Opt. Appl.* **50** 251
[28] Shao J, Lu W, Lü X, Yue F Y, Li Z F, Guo S L, and Chu J H 2006 *Rev. Sci. Instrum.* **77** 063104
[29] Shao J, Yue F Y, Lü X, Lu W, Huang W, Li Z F, Guo S L, and Chu J H 2006 *Appl. Phys. Lett.* **89** 182121
[30] Shao J, Lu W, Tsen G K O, Guo S L, and Dell J M 2012 *J. Appl. Phys.* **112** 063512
[31] Zhu L Q, Shao J, Chen X R, Li Y Q, Zhu L, Qi Z, Lin T, Bai W, Tang X D, and Chu J H 2016 *Phys. Rev. B* **94** 155201
[32] Chen X R, Zhu L Q, and Shao J 2019 *Rev. Sci. Instrum.* **90** 093106
[33] Wang F J, Liu S M, Ye X L, Zhuo N, Liu J Q, Wang L J, Zhang J C, Zhai S Q, Liu F Q, and Wang Z G 2018 *J. Nanosci. Nanotechnol.* **18** 7604
[34] Eaves L, Smith A, Skolnick M, and Cockayne B 1982 *J. Appl. Phys.* **53** 4955
[35] Klein P, Furneaux J, and Henry R 1984 *Phys. Rev. B* **29** 1947
[36] Willatzen M and Voon L C L Y 2009 *The* $\boldsymbol{k}\cdot\boldsymbol{p}$ *Method* (Berlin: Springer Science & Business Media)
[37] Wetzel C, Winkler R, Drechsler M, Meyer B, Rössler U, Scriba J, Kotthaus J, Härle V, and Scholz F 1996 *Phys. Rev. B* **53** 1038
[38] Chao C Y and Chuang S L 1992 *Phys. Rev. B* **46** 4110
[39] Sun Y, Thompson S E, and Nishida T 2010 *Strain Effect in Semiconductors: Theory and Device Applications* (Berlin: Springer Science & Business Media)
[40] Vurgaftman I, Meyer J R, and Ram-Mohan L R 2001 *J. Appl. Phys.* **89** 5815
[41] Boyd J P, Marilyn T, and Eliot P T S 2001 *Chebyshev and Fourier Spectral Methods* 2nd edn (New York: Dover Publications, Inc.)
[42] Poças L, Lopes E, Duarte J, Dias I, Lourenço S, Laureto E, Valadares M, Guimaraes P, Cury L, and Harmand J 2005 *J. Appl. Phys.* **97** 103518
[43] Yu P Y and Cardona M 2003 *Fundamentals of Semiconductors: Physics and Materials Properties* (Berlin: Springer Science & Business Media)
[44] Li J and Ning C Z 2004 *Phys. Rev. B* **70** 125309
[45] Reininger P, Schwarz B, Detz H, MacFarland D, Zederbauer T, Andrews A M, Schrenk W, Baumgartner O, Kosina H, and Strasser G 2014 *Appl. Phys. Lett.* **105** 091108
[46] Huang K and Zhu B F 1988 *Phys. Rev. B* **38** 13377